

Theranostics

2026; 16(3): 1594-1612. doi: 10.7150/thno.122226

Research Paper

CD45⁺ hybrid circulating cells may reflect tumor-immune interactions and serve as transcriptomic indicators of metastatic potential in prostate cancer

Baek Gil Kim¹.²*, Yeonsue Jang¹*, Min Gyu Kim³, Dongwook Song¹, Jungchan Jung¹, Jihee Jung¹, Ayoung Yoo¹, Jongsoo Lee¹,², Nam Hoon Cho⁴, Hyeong Jung Woo⁵, Woon-Hae Kim⁶, Hyun Young Shin⁶, Minseok S. Kim⁵,⁶, Hyun Ho Han¹.²†⊠ and Jae Young Joung³†⊠

- 1. Department of Urology, Urological Science Institute, Yonsei University College of Medicine, 50-1 Yonsei-ro, Seodaemun-gu, Seoul 03722, Republic of Korea.
- 2. Brain Korea 21 Plus Project for Medical Science, Yonsei University College of Medicine, 50-1 Yonsei-ro, Seodaemun-gu, Seoul 03722, Republic of Korea.
- 3. Center for Urologic Cancer, National Cancer Center, 323 Ilsan-ro, Ilsandong-gu, Goyang-si, Gyeonggi-do 10408, Republic of Korea.
- 4. Department of Pathology, Yonsei University College of Medicine, 50-1 Yonsei-ro, Seodaemun-gu, Seoul 03722, Republic of Korea.

 Department of New Biology, Daegu Gyeonghuk Institute of Science and Technology (DCIST), 333 Technology (DCIST), 333 Technology, Department of New Biology, Daegu Gyeonghuk Institute of Science and Technology (DCIST), 333 Technology, Department of New Biology, Daegu Gyeonghuk Institute of Science and Technology (DCIST), 333 Technology, Department of New Biology, Department of New Biology, Daegu Gyeonghuk Institute of Science and Technology (DCIST), 333 Technology, Department of New Biology, Department of New
- 5. Department of New Biology, Daegu Gyeongbuk Institute of Science and Technology (DGIST), 333 Techno Jungang-daero, Hyeonpung-eup, Dalseong-gun, Daegu 42988, Republic of Korea.
- 6. CTCELLS Inc., 216, Gaepo-ro, Gangnam-gu, Seoul 06307, Republic of Korea.
- * The authors contributed equally to this work.
- † These authors jointly supervised this work.
- 🖂 Corresponding authors: Hyun Ho Han, Email: TINTAL@yuhs.ac; Jae Young Joung, Email: urojy@ncc.re.kr.
- $\[mathcase]$ The author(s). This is an open access article distributed under the terms of the Creative Commons Attribution License (https://creativecommons.org/licenses/by/4.0/). See https://ivyspring.com/terms for full terms and conditions.

Received: 2025.07.22; Accepted: 2025.10.31; Published: 2026.01.01

Abstract

Rationale: Circulating hybrid cells expressing both epithelial and immune markers have emerged as indicators of dynamic tumorimmune interactions. This study aimed to characterize circulating hybrid cells co-expressing KRT18 (pan-cytokeratin) and PTPRC (CD45), termed KP_Pos, in metastatic prostate cancer (mPCa), and to assess their molecular features, tumor microenvironmental (TME) origins, and clinical relevance.

Methods: Imaging mass cytometry (IMC) was used to examine spatial relationships between CK⁺ tumor and CD45⁺ immune cells in metastatic prostate tissues. Single-cell RNA sequencing (scRNA-seq) datasets from mPCa were analyzed to identify KP_Pos cells and characterize their transcriptional heterogeneity across epithelial and immune lineages. Differentially expressed genes (DEGs) between KP_Pos and other cells were used to generate predictive gene signatures. Random forest (RF) and extreme gradient boosting (XGB) models were applied to evaluate metastatic classification performance, and high-performing signatures were validated in bulk RNA-seq datasets and correlated with clinical parameters.

Results: IMC revealed frequent spatial proximity between tumor and immune compartments, supporting a TME-derived hybrid phenotype. KP_Pos cells were detected across multiple immune and epithelial clusters, showing heterogeneity and enrichment of immune response and epithelial—mesenchymal transition (EMT)-related genes. Machine learning—based classifiers using KP_Pos-derived DEGs achieved high predictive accuracy (AUC \geq 0.7) for metastasis, and selected combinations further improved performance in internal validation sets. Signature scores significantly correlated with PSA and Gleason grade, and CD45 $^+$ hybrid circulating cells were more abundant in patients with advanced disease burden.

Conclusions: CD45⁺ KRT18⁺ hybrid circulating cells (KP_Pos) represent biologically distinct populations shaped by tumor–immune interactions within the TME. Their transcriptomic features and derived gene signatures may serve as biomarkers of metastatic potential and indicators of disease progression in prostate cancer. However, their causal role in metastasis and impact on survival remain to be determined.

Keywords: Prostate cancer, Circulating hybrid cells, Single-cell RNA sequencing, Metastasis prediction, CD45* KRT18* hybrid cells, Tumor-immune interaction

Introduction

Prostate cancer (PCa) is the most frequently diagnosed cancer and the fifth leading cause of cancer-related death among men worldwide, with over 1.4 million new cases and approximately 375,000 deaths each year [1]. The distinction between localized and metastatic disease is a pivotal

determinant of therapeutic decision-making, as metastatic PCa is associated with markedly worse outcomes and limited curative options [2]. Early and accurate prediction of metastasis could thus play a crucial role in improving survival and reducing treatment-related morbidity by enabling timely and tailored interventions [3].

Although many prostate cancers are initially indolent, a considerable proportion progress to aggressive phenotypes, and up to 20% of patients present with metastases at diagnosis [4]. Furthermore, among patients with localized disease, recurrence and subsequent progression to distant metastasis remain a significant clinical concern [5]. While recent advances in systemic therapies-including androgen receptor signaling inhibitors, radionuclide therapies, and immunotherapy – have transformed the management of metastatic PCa, their success hinges upon accurate risk stratification at an early stage [6]. Moreover, the advent of PSMA PET-CT has significantly altered diagnostic and therapeutic decision-making in prostate cancer, further underscoring the need for biomarkers that can complement advanced imaging modalities [7].

In this context, the identification of robust biomarkers or molecular signatures capable of predicting metastatic potential is a pressing need. Circulating tumor cells (CTCs) have emerged as a promising non-invasive biomarker of metastasis in various cancers [8]. Traditionally, CTCs are defined by the expression of epithelial markers such as cytokeratins and the absence of the pan-leukocyte marker CD45. However, recent studies have challenged this classical dichotomy by reporting CTC-like cells that co-express both epithelial and immune markers, including CD45. These hybrid phenotypes may result from epithelial-mesenchymal transition (EMT), tumor-immune cell fusion, or immune mimicry mechanisms [9-11]. One proposed mechanism underlying the emergence of such hybrid CTC-like cells is spontaneous fusion between neoplastic epithelial cells and tumor-associated macrophages. This fusion gives rise to progeny that co-express hematopoietic and epithelial markers and exhibit enhanced migratory capacity, immune evasion, and metastatic plasticity, as demonstrated in both murine models and human tumors [12].

Such phenotypically hybrid cells have been observed in several malignancies and are often enriched in patients with metastatic disease [13-15]. In prostate cancer, while CTCs are generally CD45-, recent findings suggest that CD45 expression in circulating epithelial-like cells may be associated with increased metastatic potential [11]. A similar phenomenon has been described in breast cancer,

where CD45-overexpressing tumor cells exhibit enhanced migratory and immune-evasive properties [16]. These findings indicate that the appearance of atypically expressed cells in circulation may serve as a sensitive indicator of metastatic dissemination.

Concurrently, transcriptomic analysis revolutionized the field of precision oncology by enabling comprehensive characterization of the tumor microenvironment and metastatic programs [17]. In parallel, genetic testing is now increasingly recommended in prostate cancer to refine risk stratification and guide precision treatment decisions [18]. Bulk and single-cell RNA sequencing allow for the identification of gene expression signatures linked to invasion, EMT, immune evasion, and metastasis [19, 20]. Such transcriptome-based approaches have shown promise in stratifying patients, predicting treatment response, and uncovering mechanisms of progression [21, 22].

In this study, we hypothesized that circulating tumor cell (CTC)-like populations co-expressing epithelial and immune markers may reflect underlying metastatic programs shaped by the tumor microenvironment. To test this, we conducted an integrative analysis that combines single-cell RNA sequencing (scRNA-seq)-based signature discovery from primary prostate tumors with validation in bulk RNA-seq datasets from metastatic prostate cancer tissues. By evaluating the predictive value of these transcriptomic signatures for metastatic status, we aim to identify robust biomarkers associated with tumor aggressiveness. We note that such associations do not imply direct causation, which would require functional validation beyond the scope of this study. This approach provides a foundation for a novel biomarker framework aligned with personalized and metastasis-informed management strategies prostate cancer.

Materials and Methods

Sample acquisition

Peripheral blood mononuclear cells (PBMCs) and tissue samples were collected from prostate cancer patients as part of a study approved by the Institutional Review Board of Severance Hospital, Yonsei University College of Medicine (IRB numbers: 4-2022-0710, 4-2021-0276). All participants provided written informed consent after being appropriately informed that their peripheral blood and tissue samples would be used for research purposes. Peripheral blood samples (5 mL) were obtained from 82 patients via venipuncture using a 21-gauge needle and collected into EDTA-coated Vacutainer tubes (Becton, Dickinson and Company, Franklin Lakes, NJ)

for circulating cell analysis. Peripheral blood mononuclear cells (PBMCs) were isolated from seven patients with metastatic prostate cancer (M1 stage) for single-cell RNA sequencing (scRNA-seq) analysis. For comparative purposes, biopsy tissues from five additional patients with clinically and radiographically confirmed metastatic prostate cancer (M1 stage) were also collected and processed for scRNA-seq. Because patient consent prohibited paired blood-tissue collection, the PBMC and biopsy cohorts were analyzed independently. In addition, biopsy specimens from 234 prostate cancer patients—including both non-metastatic (M0) and metastatic (M1) cases—were subjected to bulk RNA sequencing.

Circulating cell isolation

Circulating cell isolation was performed using the CTCeptor system (CTCELLS, Daegu, South Korea), a fully automated Continuous Centrifugal Microfluidics-Circulating Tumor Cell Disc (CCM-CTCD) platform [23, 24]. This system employs a rotating microfluidic disc to separate blood components based on their density. A synchronized laser-controlled motor activates an internal valve to release a thin layer enriched with tumor-derived and white blood cells into a designated chamber, where circulating cells are selectively captured through antibody-based surface binding. The isolated cells were subjected to immunofluorescence staining using following antibodies: anti-pan-cytokeratin (PanCK; eBioscience, San Diego, CA), anti-CD45 (BioLegend, Diego, CA), and San prostate-specific antigen (PSA; Invitrogen, Waltham, MA). Stained cells were imaged and analyzed to distinguish epithelial-derived cells (PanCK+/CD45-), immune-origin cells (CD45⁺), and hybrid phenotypes (PanCK⁺/CD45⁺), reflecting the cellular heterogeneity of circulating populations in prostate cancer.

Imaging mass cytometry

Formalin-fixed, paraffin-embedded (FFPE) prostate tissue sections from 21 tissue microarrays (TMAs) of metastatic prostate cancer were deparaffinized, rehydrated, subjected to antigen retrieval, and blocked with 3% BSA. The slides were then incubated with metal-conjugated antibodies labeled using Maxpar X8 Antibody Labeling Kits (Standard BioTools, South San Francisco, CA), purified, and quantified using NanoDrop spectrophotometry (Thermo Fisher Scientific, Waltham, MA), followed by storage at 4°C until use. A Standard BioTools-verified antibody panel targeting tumor and immune-related markers-including cytokeratin, CD45, CD14, and CD16-was applied for staining. Imaging Mass Cytometry (IMC) was performed using the Hyperion Imaging System (Standard BioTools), with laser ablation and data acquisition conducted at JCBio (Seoul, South Korea). Regions of interest (1000 × 1000 um) were selected based on tissue morphology, and the acquired data were processed using CvTOF software v7.0 (Standard BioTools, South San Francisco, CA). Image quality was assessed prior to exporting the data as multilayer OME-TIFF files, which were analyzed using HALO Imaging Analysis Software (v3.5, Indica Labs, Albuquerque, NM). The Highplex FL module was used for cell segmentation and marker quantification, while spatial tissue analyses - including nearest neighbor and proximitybased interaction mapping-were performed to characterize tumor-immune interactions. Co-registration of serial sections and the generation of density heatmaps enabled detailed spatial visualization of immune and epithelial cell populations. Morphometric quantification of CK+CD45+ double-positive cells was performed using cell segmentation masks generated in HALO. Cell and cytoplasmic area distributions were binned (10 µm² per bin), and bin-wise percent values were calculated for each group. To enable quantitative comparison across groups, cumulative proportions ("AUC percent") were computed as the sum of percent values within the defined small-size range (≤250 µm²), representing the relative enrichment of smaller cells.

RNA sequencing

Single-cell RNA sequencing

Freshly obtained primary tumor biopsy specimens from metastatic prostate cancer patients (M1 stage) were processed to generate single-cell suspensions. Enzymatic dissociation was performed using in-house optimized protocols developed by DCGEN (Seoul, South Korea). Following filtration through a 40 µm cell strainer (Corning, Corning, NY) and viability assessment using an automated cell counter (Countess II, Thermo Fisher Scientific, Waltham, MA), single cells were encapsulated and barcoded using the Chromium Controller system (10x Genomics, Pleasanton, CA) operated at Macrogen (Seoul, South Korea). cDNA synthesis, amplification, and library construction were conducted according to the manufacturer's protocol (10x Genomics). Libraries were quality-checked with a Bioanalyzer (Agilent Technologies, Santa Clara, CA) and a Qubit fluorometer (Thermo Fisher Scientific, Waltham, MA), and sequenced on Illumina NovaSeq 6000 or NextSeq 2000 platforms (Illumina, San Diego, CA). The raw sequencing data were processed using Cell Ranger software (10x Genomics) to generate gene expression matrices for downstream analyses, including tumor

microenvironment (TME) characterization ligand-receptor interaction mapping. Peripheral blood mononuclear cells (PBMCs) were isolated from seven patients with metastatic prostate cancer (M1 stage) and subjected to single-cell RNA sequencing (scRNA-seq) to profile circulating immune-cell transcriptomes. After cell isolation and viability assessment, single-cell encapsulation and barcoding were performed using the Chromium Controller system (10x Genomics, Pleasanton, CA). Library preparation, including cDNA synthesis amplification, was conducted according to the manufacturer's protocol. Sequencing was performed by Eyeoncell (Gwangju, South Korea) on Illumina NovaSeq 6000 or NextSeq 2000 platforms (Illumina, San Diego, CA). Raw sequencing data were processed using Cell Ranger software (10x Genomics) to generate gene-cell count matrices for downstream analyses.

Bulk RNA sequencing

Total RNA was extracted from biopsy tissues using TRIzol reagent (Thermo Fisher Scientific, Waltham, MA) or the RNeasy Mini Kit (Qiagen, Hilden, Germany). RNA integrity was verified using a Bioanalyzer (Agilent Technologies, Santa Clara, CA), and RNA concentrations were measured using a Qubit fluorometer (Thermo Fisher Waltham, MA). Only samples with an RNA Integrity Number (RIN) greater than 7.0 were used for library preparation with the TruSeq Stranded mRNA Library Prep Kit (Illumina, San Diego, CA). Sequencing was performed on the Illumina NovaSeg 6000 or NextSeg 2000 platforms (Illumina, San Diego, CA) using 100-150 bp paired-end reads, with a target depth of 20-50 million reads per sample. Raw reads were aligned to the reference genome using STAR or HISAT2, and gene expression was quantified using featureCounts or HTSeq-count.

Single-cell transcriptomic analysis and differential gene expression

Single-cell RNA-seq data were analyzed using R (v4.3.2) and the Seurat package. For integrated analyses, scRNA-seq datasets from five metastatic prostate cancer cases were merged using the anchor-based integration workflow implemented in Seurat v4. Briefly, each dataset was log-normalized, and the top 2,000 variable features were identified. Integration calculated anchors were using FindIntegrationAnchors with default parameters, and the datasets were aligned into a shared expression IntegrateData, which corrects space via patient-specific batch effects while preserving

biological variability. This integration enabled direct comparison of identical cell types across patients, enhanced the detection of rare populations (e.g., KP Pos cells), and improved the robustness of downstream clustering, annotation, and differential expression analyses. Cell type annotation was performed using six complementary approaches: (1) SingleR-based methods, including (i) cell-level annotation using the HumanPrimaryCellAtlasData reference, (ii) cluster-level majority voting, defined as assigning the most frequent SingleR-derived cell-type label within each Seurat-defined cluster, and (iii) cluster-to-cell-type mapping; (2) CellTypist-based annotation using the Immune_All_Low pretrained model; (3) canonical marker-based annotation using curated cell type-specific gene sets; and (4) cell subtype-specific marker scoring using lineagerelevant markers for regulatory, cytotoxic, exhausted, memory, and helper T cells, B-cell subsets, macrophages, and epithelial cells. Marker gene sets used for annotation are listed in Supplementary Tables S7-1 (cell types) and S7-2 (cell subtypes). In this study, no single annotation approach was designated as the "gold standard." Instead, all six methods were applied to capture complementary perspectives on cell identity, acknowledging that each can yield distinct yet biologically meaningful results. For downstream analyses and visualization in the main selected the SingleR we cluster-level majority-voting annotation as the representative strategy because it provided clearer cluster separation in two-dimensional embeddings and minimized figure complexity. This choice was made solely for presentation clarity and does not indicate analytical preference or bias. To ensure interpretability and reproducibility, all differential expression analyses and subsequent signature construction steps were based on a unified DEG pool that combined the results from all annotation approaches, thereby incorporating both overlapping and method-specific DEGs. KP_Pos cells were defined as those co-expressing KRT18 and PTPRC (normalized expression > 0.1), with all other cells categorized as "Others." DEG analysis comparing KP_Pos versus Others was conducted using the Wilcoxon rank-sum test implemented in Seurat's FindMarkers function, applying a log₂ fold-change threshold ≥ 0.25 and requiring expression in at least 10% of cells per group. Significant DEGs were selected based on an adjusted p-value ≤ 0.05. Two DEG strategies were performed: (i) cluster-based analysis within our metastatic prostate cancer scRNA-seq dataset, and metastasis-specific analysis incorporating benign and localized prostate cancer samples from GSE193337.

Cell-cell interaction analysis

Cell-cell communication was analyzed using the CellChat R package (v1.6.1). Raw count matrices from Seurat-integrated single-cell RNA-seq data of PBMCs from metastatic prostate cancer patients were merged into a unified Seurat object. Cell types were annotated using SingleR with the HumanPrimaryCellAtlasData reference, and the resulting labels were incorporated into the CellChat metadata. A CellChat object was constructed using the merged count matrix and cell-type annotations and analyzed with the CellChatDB.human ligand-receptor database. Overexpressed genes and interactions were identified using the functions identifyOverExpressedGenes() identifyOverExpressedInteractions(). Communication probabilities were computed via computeCommunProb() computeCommunProbPathway(), considering only cell types containing ≥10 cells. The resulting network strengths were aggregated with aggregateNet() and visualized using circular and heatmap layouts. Sender-receiver (incoming/outgoing) analyses were performed for six major immune populations-monocytes, macrophages, T cells, NK cells, B cells, and CMPs-to quantify intercellular signaling strength and relative communication topology.

Signature-based classification and model evaluation

To identify transcriptomic signatures predictive of metastasis (M0 vs. M1), we implemented a machine learning workflow based on gene expression-derived features. Each signature was evaluated using a three-way data partitioning strategy (training/ validation/test) with five different random seeds to ensure robustness and reproducibility. Model training and validation were performed using random forest (RF) and extreme gradient boosting (XGB), and performance was assessed by calculating AUC, PR AUC, accuracy, sensitivity, specificity, precision, and F1-score. To control for overfitting, signatures were categorized into four levels (none, mild, moderate, severe) based on discrepancies between training and test set performance; only signatures classified as None in the overfitting-level analysis were used for downstream analysis. A composite score was calculated by z-transforming PR AUCs from both RF and XGB models and summing them, enabling robust ranking of consistently high-performing signatures. Signatures with AUC \geq 0.7 in the test set were further applied to bulk RNA-seq data for M-stage (M0 vs. M1) prediction. This cutoff of 0.7 was selected because it is widely regarded as the lower bound for clinically meaningful discrimination, balancing sensitivity and

specificity beyond random chance. The threshold has also been frequently adopted in prior biomarker studies to ensure comparability across studies and to exclude weak predictors. Given the class imbalance in our dataset, PR-AUC ≥ 0.7 in the test set was used as the primary criterion, ensuring that only robustly predictive signatures were advanced to downstream analysis. To assess whether predictive performance could be improved through integration, combinations of top-ranked signatures were tested using logistic regression, RF, and XGB with repeated stratified cross-validation across five seeds. Model performance was compared using mean ROC AUC, PR AUC, accuracy, and F1-score, and the final composite models were evaluated for associations with clinical features.

M0/M1 prediction and performance evaluation

For M-stage classification (M0 vs. M1), model performance was assessed using standard binary classification metrics. Predicted probabilities from RF and XGB models were converted into class labels using a default threshold of 0.5, unless otherwise optimized based on PR AUC. The following evaluation metrics were calculated: accuracy = (TP + TN) / (TP + TN + FP + FN), sensitivity = TP / (TP +FN), specificity = TN / (TN + FP), precision = TP / TP(TP + FP), and F1-score = $2 \times (precision \times sensitivity)$ / (precision + sensitivity). Additionally, area under the receiver operating characteristic curve (ROC AUC) and precision-recall curve (PR AUC) were computed to assess overall discriminative power, particularly under class imbalance. All metrics were averaged across five random seeds for robust comparison between individual signatures and signature combinations.

Correlation analysis with clinical variables

To assess the clinical relevance of circulating cell phenotypes and gene expression-based prediction scores, we performed correlation analyses with key clinical parameters including age, PSA level, Gleason score, and TNM staging. For circulating cell phenotypes defined by CD45 expression status (CD45⁺ and CD45⁻), Pearson correlation coefficients were calculated and visualized using Microsoft Excel (Microsoft Corporation, Redmond, WA). combined signature scores derived from top-ranked gene sets, Spearman rank correlation was computed in R using the cor.test() function. Clinical variables were numerically encoded, and results were visualized using ggplot2-based bubble plots, where color scale represented correlation strength and direction, and circle size indicated statistical significance $(-\log_{10}(p\text{-value}))$.

Statistical analysis

All statistical analyses were performed using GraphPad Prism (GraphPad Software, La Jolla, CA) and R (version 4.3.2). Gene expression differences between groups were assessed using two-tailed unpaired Student's t-tests, assuming equal variance unless otherwise specified. Correlation analyses in RNA-seq datasets were conducted using Pearson's correlation coefficient. For correlation between gene signature-based predictions and clinical parameters, Spearman's rank correlation was used when the data were not normally distributed or were ordinal in nature. A p-value less than 0.05 was considered statistically significant. Statistical significance was denoted by asterisks as follows: $p \le 0.05$ (*), $p \le 0.01$ (**), and $p \le 0.001$ (***). Where applicable, multiple testing correction was performed using Benjamini-Hochberg false discovery rate (FDR) method. All visualizations were generated using R packages including ggplot2, and significance markers were applied accordingly in plots and tables.

Results

CD45 expression and characterization of CTC-like cells in metastatic prostate cancer

We investigated CD45 expression in circulating tumor cell (CTC)-like populations to define the cellular identity of CD45⁺ subsets through immunostaining, **PBMC** clustering, transcriptomic profiling of metastatic prostate cancer samples. CTC-like cells were detected in the majority of 82 metastatic cases and were stratified by tumor burden, overall survival, and TNM stage (Figure 1A). Their abundance correlated with higher tumor load and advanced disease (Supplementary Figure S1-1A), although CD45 expression itself showed no significant association with clinical parameters (Supplementary Figure S1-1B). Quantification revealed that a substantial portion of cytokeratin+ CTC-like cells co-expressed CD45 (Figure 1B-a,b). Immunofluorescence further confirmed CD45⁺/PanCK⁺ dual staining in patient-derived CTC-like cells, with PSA signals often overlapping CD45 (Supplementary Figure S1-1C). Single-cell transcriptomic profiling of PBMCs from seven M1-stage patients identified diverse lineages – T cells, B cells, NK cells, monocytes, CMPs, erythroblasts, and platelets (Figure 1C-a). Within these, a rare subset of KRT18+ PTPRC+ (KP_Pos) cells was detected, primarily among T and B cells (Figure 1C-b), comprising 0.867% (561 of 64,693) of total PBMCs (Figure 1C-c). Annotation using multiple approaches – SingleR (Supplementary Figure S1-2-1), cluster-to-cell-type (S1-2-2), CellTypist (S1-2-3),

canonical marker (S1-2-4), and curated subtype markers (S1-2-5) - consistently confirmed immune lineage identities. Independent analyses validated reproducibility across seven PBMC (Supplementary Figures S1-3-1 and S1-3-2-1 to S1-3-2-7). Differential expression analysis comparing KP_Pos and other cells (Figure 1D; Supplementary Table S1-1) revealed upregulation of KRT18 and multiple ribosomal protein genes (RPS12, RPS13, RPL30, RPS3A, RPL11, RPL32, RPS8, RPS23, RPS14, RPL5), indicating enhanced translational activity and reprogramming. partial epithelial-like regulated genes included mitochondrial oxidative phosphorylation-related transcripts (MT-CO1, MT-CO2, MT-CO3, MT-ATP6, MT-ND5) regulators such as PARP8, RABGAP1L, UTRN, ZEB2, consistent with metabolic rewiring and reduced mitochondrial respiration. T cells, accounting for 86.3% of all KP_Pos cells (484/561), were presented as the representative subset for primary DEG analysis, while B cells, monocytes, and platelets showed analogous yet distinct transcriptional changes (Supplementary Figure S1-4; Supplementary Table S1-1). For clarity and consistency, the SingleR cluster-level majority-voting annotation was adopted as the representative framework in the main text. Alternative annotation strategies – CellTypist-, subtype marker-, canonical marker-, unsupervised cluster-based methods (Supplementary Figures S1-2-1 to S1-2-5) – produced complementary DEG lists (Supplementary Tables S1-2 to S1-6). All DEGs were integrated into a unified DEG pool, ensuring that downstream analyses captured the full transcriptional spectrum for signature development.

Characterization of CK+CD45+ cells in primary tumors reveals spatial, morphological, and signaling features linked to CTC-like phenotypes

To explore the origin and identity of CK⁺CD45⁺ circulating tumor cell (CTC)-like populations observed in peripheral blood (Figure 1), we analyzed metastatic prostate cancer tissues using Imaging Mass Cytometry (IMC) and single-cell RNA sequencing. CK-high tumors exhibited close spatial proximity between CK⁺ and CD45⁺ cells and enriched EMT-like features (Figure 2A). Tumors were stratified into three groups by pan-CK expression: CK-high (G1), CK-medium (G2), and CK-low (G3). IMC imaging revealed dense colocalization of CK⁺ and CD45⁺ cells in G1 tumors (Figure 2A-a), with progressively separated patterns in G2 and G3. Quantitative analysis confirmed significantly shorter CK-CD45 distances in G1 (p < 0.001) and higher frequencies of CK⁺VIM⁺ EMT-like cells (Figure 2A-b,c).

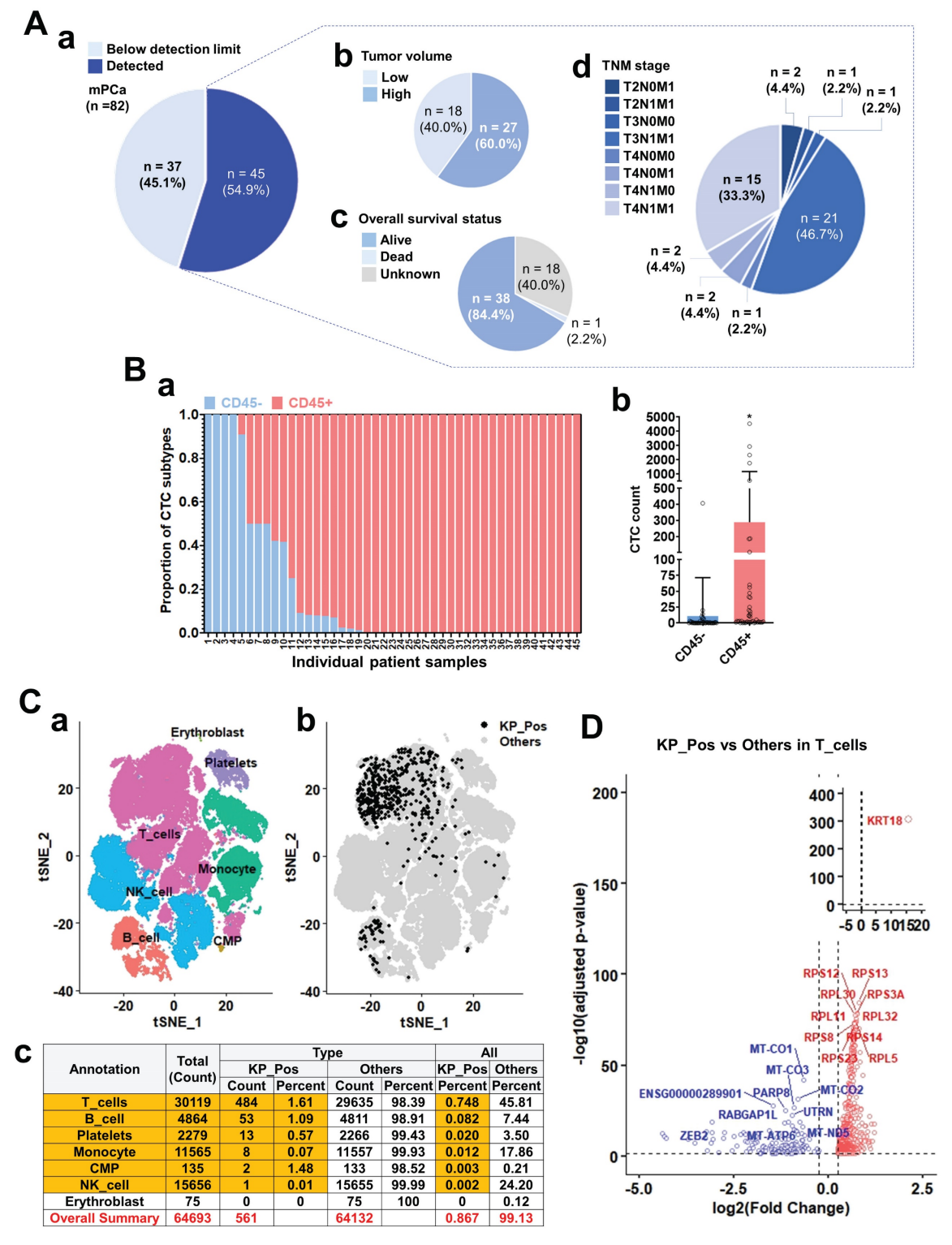


Figure 1. CD45 expression analysis and characterization of circulating tumor cell (CTC)-like cells in metastatic prostate cancer. (A) Overview of CTC-like cell detection and associated clinical parameters in metastatic prostate cancer patients (n = 82). (a) Distribution of patients based on CTC-like cell levels above or below the detection limit. (b) Tumor volume classification in patients with detectable CTC-like cells. (c) Overall survival status of patients with detectable CTC-like cells. (d) TNM staging distribution among patients with detectable CTC-like cells. (B) Analysis of CD45 expression in cytokeratin-positive CTC-like cells. (a) Patient-wise proportion of CD45* and CD45* populations among cytokeratin-positive CTC-like cells. (b) Quantification of cytokeratin-positive CTC-like subsets stratified by CD45 expression status. (C) Clustering, mapping, and quantitative summary of peripheral blood mononuclear cells (PBMCs) integrated from seven metastatic prostate cancer (M1 stage) patients. (a) t-SNE (t-distributed Stochastic Neighbor Embedding) plots showing clustering and annotation of PBMCs based on majority-voting classification. Major immune populations including T cells, B cells, NK cells, monocytes, common myeloid progenitors (CMPs), erythroblasts, and platelets were identified. (b) Distribution of double-positive KRT18* (cytokeratin) and PTPRC* (CD45) cells, referred to as KP_Pos cells, within the PBMC population. KP_Pos cells (black) and other cells (gray) are visualized across annotated clusters on the t-SNE map. (c) Summary table showing the number and proportion of KP_Pos and other cells within each annotated population. Among 64,693 PBMCs, 561 cells (0.867%) were classified as KP_Pos (highlighted in red), whereas 64,132 cells (99.13%) were classified as others. The overall summary row is highlighted in yellow for emphasis. (D) Differentially expressed genes (DEGs) of KP_Pos versus other cells within the T-cell population from PBMCs of seven M1-stage prostate cancer patients. Genes were ranked

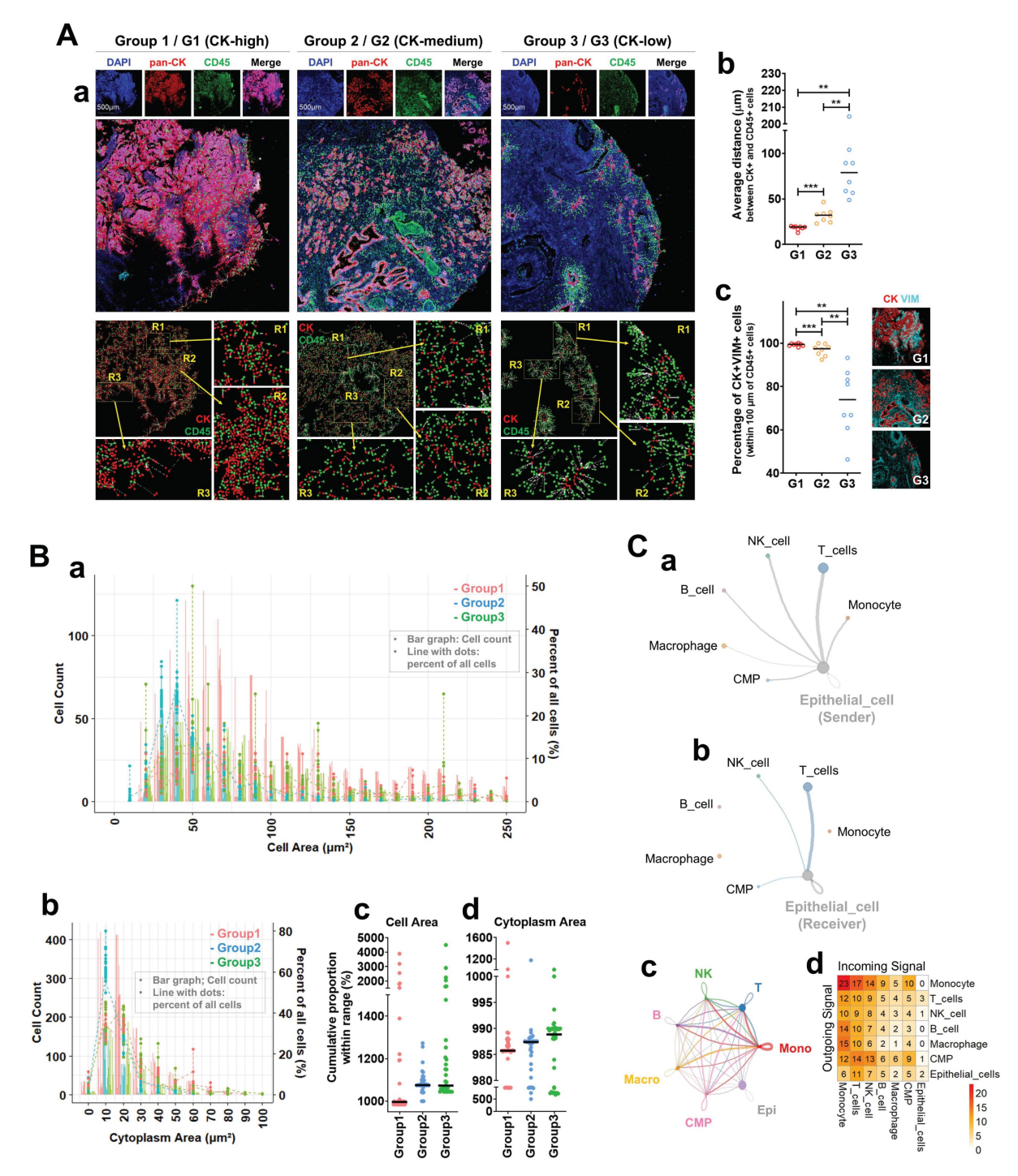


Figure 2. Spatial and transcriptomic characterization of CK*CD45* cells in primary tumors suggests a microenvironmental basis for CTC-like phenotype emergence. (A) Spatial analysis of CK+ and CD45+ cells using Imaging Mass Cytometry (IMC). (a) Representative IMC images of metastatic prostate cancer tissues categorized into three groups based on pan-CK expression levels. Top: Individual and merged fluorescence channels showing DAPI (blue), pan-CK (red), and CD45 (green) staining in Group I (G1: CK-high), Group 2 (G2: CK-medium), and Group 3 (G3: CK-low). Middle: Composite marker overlays and multiplexed spatial distribution maps at the single-cell level. Bottom: Spatial cell mapping with segmentation showing the distribution of CK+ (red) and CD45+ (green) cells. Enlarged regions (R1-R3) highlight areas of spatial proximity between these two populations. (b) Quantification of the average distance (µm) between CK+ and CD45+ cells across the three groups. (c) Proportion of CK+VIM+ cells—indicative of epithelial–mesenchymal transition (EMT)-like features—among total CK+ cells. Statistical significance: *p < 0.05; **p < 0.01; ***p < 0.001. (B) Morphometric profiling of CK⁺CD45⁺ double-positive cells. (a) Distribution of total cell area (µm²) of CK⁺CD45⁺ double-positive cells in Group 1 (red), Group 2 (blue), and Group 3 (green). Absolute counts are shown as bar graphs, while relative frequencies (%) are overlaid as line plots with dots. To enhance visibility, values are truncated at 250 µm². The full distribution across the complete range, separated into Count and Percent plots, is provided in Supplementary Figure S2-I-I-I. (b) Distribution of total cytoplasm area within the restricted range, shown separately as Count and Percent plots in Supplementary Figure S2-1-1-2. (c) Cumulative proportions of cells within the defined small-size range for total cell area across the three groups. (d) Cumulative proportions of cells within the defined small-size range for cytoplasmic area across the three groups. Black horizontal lines indicate median values. Quantitative summaries of AUC and global statistics for cell and cytoplasmic area are provided in Supplementary Tables S2-1 to S2-4. (C) Intercellular communication analysis centered on epithelial cells using single-cell RNA sequencing. (a, b) Circle plots showing outgoing (a) and incoming (b) signaling interactions of epithelial cells with major immune populations. (c) Circle plot summarizing the overall intercellular communication network among epithelial cells and immune populations, including T cells, NK cells, B cells, macrophages (Macro), monocytes (Mono), and CMPs. (d) Heatmap displaying the overall strength of intercellular communication between epithelial and immune cell populations. All annotations were harmonized with those in Figure 1C. Detailed outgoing and incoming communication profiles for each cell lineage are provided in Supplementary Figures S2-2-1-1 to S2-2-2.

Morphometric analysis of CK+CD45+ double-positive cells (Figure 2B-a,b) revealed broader size distributions in G1 but a left-shift toward smaller cell and cytoplasmic areas in cumulative proportion plots (Figure 2B-c,d). Summaries of these parameters are provided in Supplementary Tables S2-1 to S2-4, listing cumulative and global size statistics for each CK-defined group. Supplementary Figures S2-1-1-1 and S2-1-1-2 display full distributions of total cell area from Figure 2B-a as count and percent plots (≤ 250 μm²), while Supplementary Figure S2-1-2 shows the corresponding cytoplasmic distributions. These data indicate enrichment of compact, densely distributed immune-epithelial hybrid cells in CK-high tumors. Intercellular communication analysis based on single-cell RNA sequencing of M1-stage tumor biopsies revealed extensive epithelial signaling with multiple immune populations (Figure 2C-a,b). The strongest bidirectional interactions were observed between epithelial cells and T cells, defining a dominant epithelial-T cell signaling axis. The global network (Figure 2C-c) confirmed that epithelial cells were highly integrated with T, NK, B, monocyte, macrophage, and CMP lineages. This network suggests that intense epithelial-T cell cross-talk serves as a central communication hub driving hybrid (CD45+/KRT18+, KP_Pos) cell formation within the tumor microenvironment. To ensure lineage consistency with Figure 1C, platelets were excluded to avoid signals from circulating components [25], although platelet infiltration into solid tumors has been reported [26]. Macrophages were included due to their myeloid lineage continuity with circulating monocytes, which can differentiate into tissue macrophages [27]. In the directional interaction heatmap (Figure 2C-d), rows represent signal senders and columns receivers. Monocytes showed the highest outgoing signaling toward epithelial cells, whereas epithelial cells displayed moderate reciprocal signaling to T cells and monocytes. Among all pairs, epithelial-T cell interactions remained the most balanced and sustained. Detailed outgoing and incoming signaling profiles are presented in Supplementary Figures S2-2-1-1 S2-2-2-2. to Supplementary Figure S2-2-1-1 depicts outgoing signals from T, B, NK, monocyte, macrophage, CMP, and epithelial populations, with simplified circle plots in Supplementary Figure S2-2-1-2. Incoming networks for the same populations are shown in Supplementary S2-2-2-1 and S2-2-2-2, highlighting **Figures** lineage-specific signal reception. These results collectively extend Figure 2C by visualizing directional and quantitative aspects of immuneepithelial communication in metastatic prostate

cancer. Finally, quantitative IMC analysis further confirmed CK and CD45 co-expression at the single-cell level (Supplementary Figure S2-3). Scatter plots display CK and CD45 signal intensities from thousands of cells across three CK-defined groups, with three representative cases per group (e.g., G1-1, G1-2, G1-3). Each point represents an individual cell. Together, these IMC and transcriptomic analyses demonstrate spatial, morphological, and signaling evidence supporting the presence and functional relevance of hybrid immune-epithelial (CK+CD45+) populations in metastatic prostate cancer.

Distribution and transcriptional features of KP_Pos cells in the metastatic tumor microenvironment

To explore the distribution of KP Pos cells across cell types, we analyzed single-cell transcriptomic profiles from five metastatic prostate cancer biopsy samples, which were entirely independent of the PBMC cases in Figure 1 (no overlap between bloodand tissue-derived datasets). Cluster-level annotation via majority voting identified epithelial, immune, and stromal lineages (Figure 3A-a). Expression maps of KRT18 and PTPRC (Figure 3A-b,c) showed that KP_Pos cells were broadly distributed across the t-SNE embedding (Figure 3A-d). Quantification across annotated lineages revealed that, among the six immune subsets previously detected in PBMCs, KP_Pos cells were most frequent in T cells, macrophages, NK cells, B cells, monocytes, and CMPs (Figure 3B). This distribution pattern was consistently reproduced using six complementary annotation strategies: cell-level annotation (Supplementary Figure S3-1), cluster-level majority voting (S3-2), cluster-to-cell-type mapping (S3-3), CellTypist-based cell subtype annotation (S3-4), marker-based immune annotation (S3-5), and subtype-specific marker-based annotation (S3-6). In all methods, populations enriched for KP_Pos cells – particularly T cells, macrophages, NK cells, B cells, monocytes, and CMPs—were highlighted in orange accompanying summary tables. To define molecular characteristics of KP_Pos cells, differential gene expression analysis was performed between KP_Pos and Other cells within the six major immune lineages. Volcano plots revealed distinct sets of significantly upregulated genes in KP Pos cells across lineages, with the highest numbers observed in CMPs, macrophages, and T cells (Figure 3C). Complete gene lists for all annotation strategies are provided in Supplementary Tables S3-1 to S3-6.

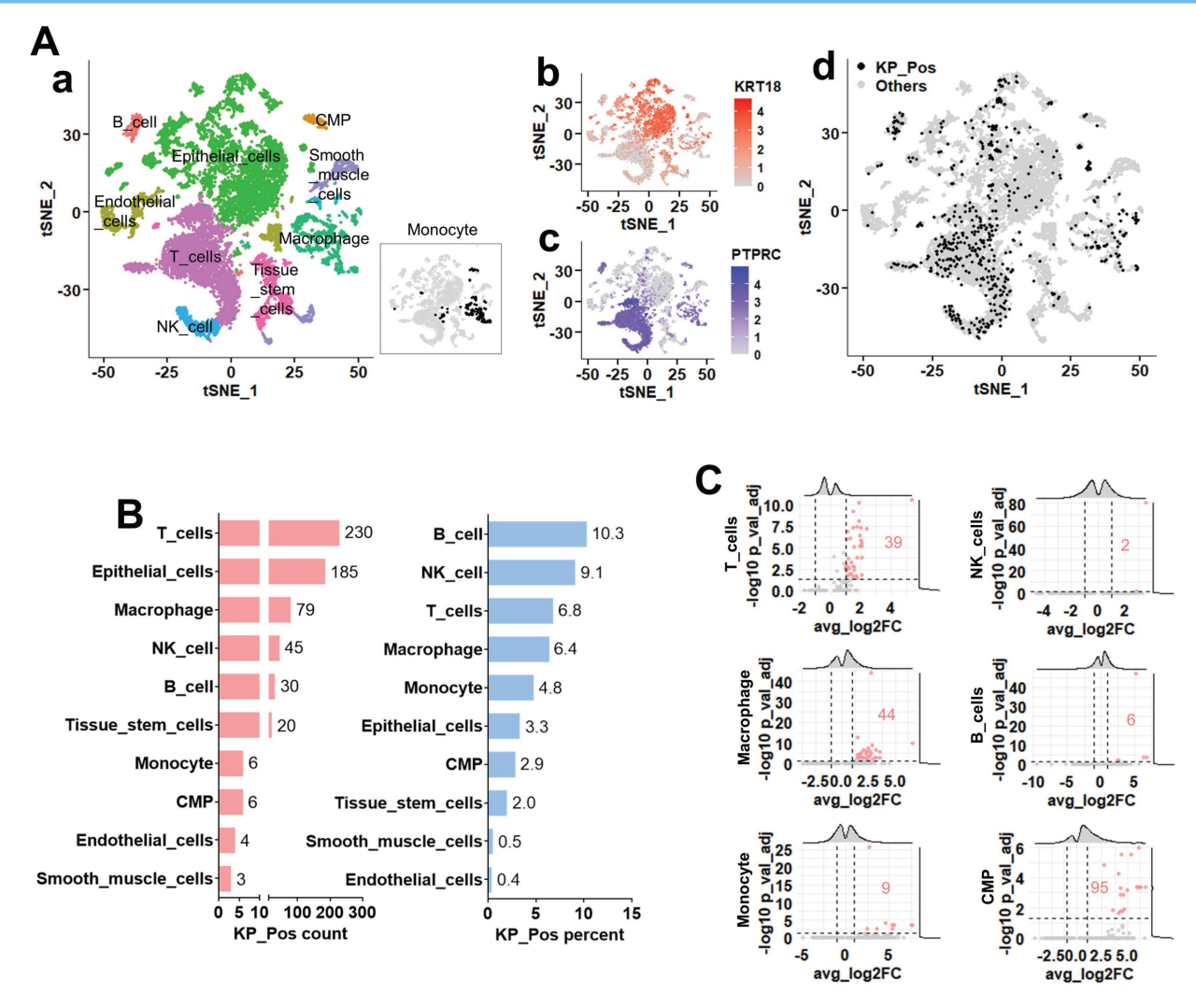


Figure 3. Single-cell transcriptomic analysis of metastatic prostate cancer reveals the distribution and transcriptional features of KP_Pos (KRT18*PTPRC*) cells. (A) Cell clustering and annotation. (a) Cell identities assigned by majority voting across Seurat clusters; since monocytes were not clearly resolved in the clustering, their distribution is separately highlighted in the inset. (b-c) Feature plots showing expression of KRT18 (b) and PTPRC (c). (d) Distribution of KP_Pos cells (KRT18*PTPRC*) projected onto the t-SNE map. (B) Cell type composition of KP_Pos cells. Number and proportion of KP_Pos cells per annotated cell type. (C) Differential gene expression in KP_Pos versus others. Volcano plots showing differentially expressed genes between KP_Pos and other cells across six major immune cell types (T cells, NK cells, macrophages, B cells, monocytes, and CMPs). Red numbers indicate the count of significantly upregulated genes (adjusted p < 0.05, log2FC > 1).

Single-cell transcriptomic profiling identifies metastasis-specific cellular and molecular features of KP_Pos cells

To identify metastasis-specific alterations in the composition and gene expression of KP_Pos (KRT18+PTPRC+) cells, we conducted an integrated single-cell transcriptomic analysis of benign, primary, and metastatic prostate cancer tissues. Seurat-based majority voting confirmed the presence of KP_Pos cells across all stages (Figure 4A). In t-SNE projections (Figure 4B-a-c), KP_Pos cells showed lineage- and stage-dependent distribution patterns: T cells (red outline) exhibited a progressive increase from benign to metastatic states; epithelial cells (sky blue, upper cluster) decreased gradually, while another epithelial subset (purple, lower cluster) displayed a biphasic pattern (primary > metastatic > benign). Monocytes

(green outline) demonstrated a marked enrichment in tumors, whereas CMPs, primary macrophages, and NK cells showed minimal stage-specific variation. Quantitative comparison revealed a lineage shift in KP_Pos composition across disease stages, with macrophage-derived KP_Pos populations predominating in metastatic tumors and CMP-associated KP_Pos cells enriched mainly in primary tissues (Figure 4C). Results from five complementary reference-based cell-level annotation methods, consistent with the Seurat-based majorityvoting annotation, are summarized in Supplementary Tables S4-1-1 to S4-1-6 (table only, without figure presentation due to overlap with Figure 3). To further characterize KP_Pos heterogeneity in metastasis, we analyzed subtype distributions within three major compartments. In epithelial cells, KP_Pos cells were enriched in the Epithelial_EMT subtype

(Supplementary Figure S4-1). Within T cells, they were predominantly associated with T_Memory and T_Exhausted phenotypes (Supplementary Figure S4-2). Among monocytes, KP_Pos cells were less abundant in metastasis but enriched in the Mono_NonClassical subtype during earlier stages (Supplementary Figure S4-3). Differential gene expression analysis comparing metastatic, primary,

and benign KP_Pos cells across six immune lineages—T cells, NK cells, B cells, macrophages, monocytes, and CMPs—revealed lineage-specific transcriptional changes (Figure 4D). Distinct upregulated gene sets were most prominent in T cells and CMPs, indicating activation of metastatic programs in these populations (Supplementary Tables S4-2-1 to S4-2-6).

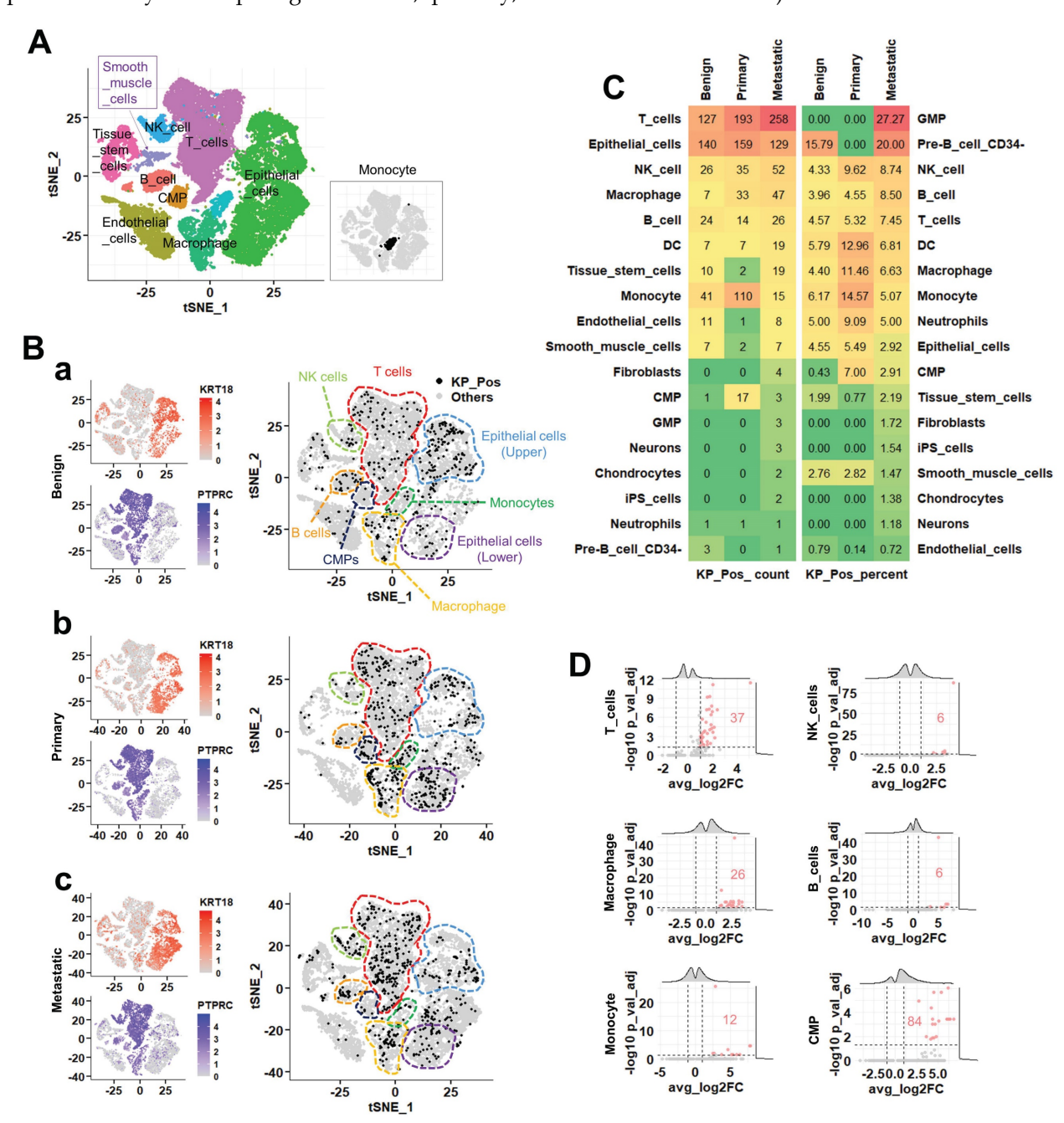


Figure 4. Integrated single-cell transcriptomic analysis of KP_Pos populations across benign, primary, and metastatic prostate cancer. (A) Clustering of integrated single-cell data. Annotation based on majority voting across Seurat-defined clusters. Since monocytes were not clearly resolved in the clustering, their distribution is separately highlighted in the inset (rectangular box) of the t-SNE map. (B) Distribution of KP_Pos and others in t-SNE space and marker gene expression. Left: Expression levels of KRT18 and PTPRC across benign (top), primary (middle), and metastatic (bottom) samples. Right: Distribution of KP_Pos (KRT18*PTPRC*) and other cells in t-SNE space for each disease stage (a, benign; b, primary; c, metastatic). Dashed boundaries delineate major cell lineages: T cells (red), NK cells (light green), B cells (orange), macrophages (yellow), monocytes (green), CMPs (navy), and epithelial cells (sky blue and purple). KP_Pos cells (black dots) were broadly distributed across multiple immune and epithelial lineages. (C) Cell type composition of KP_Pos cells. Heatmap showing the number (left) and percentage (right) of KP_Pos cells across cell types in benign, primary, and metastatic samples. Color intensity reflects values from low (green) to high (red). (D) Metastasis-specific differentially expressed genes in KP_Pos cells. Volcano plots displaying DEGs in KP_Pos cells from metastatic samples compared to benign and primary samples within six major immune cell types: T cells, NK cells, B cells, Macrophages, Monocytes, and CMPs. Significantly upregulated genes are marked in red (adjusted p < 0.05 and |log₂FC| > 0.25). DEG counts are annotated within each plot.

Construction and evaluation of scRNA-seqbased gene signatures for M0/M1 classification

To identify gene signatures predictive of metastatic status (M0 vs. M1), we implemented a multi-step workflow encompassing marker selection, model development, and performance evaluation (Figure 5A). Differentially expressed genes (DEGs) were collected from two major sources: (i) clusterderived DEGs obtained from diverse annotation methods (SingleR at cluster- and cell type-levels, cluster-level majority voting, cluster-to-cell-type mapping, CellTypist, and marker-based references) and (ii) metastasis-specific DEGs identified by comparing epithelial cells from metastatic, benign, and primary prostate tissues. In total, 7,488 cluster-derived and 6,408 metastasis-specific DEGs were compiled, encompassing epithelial, immune, and stromal populations (Figure 5B-a,b). All DEGs – including those distinguishing KP_Pos versus other cells across immune lineages-were pooled to construct candidate marker sets for M0/M1 classification. Each marker set was evaluated through three-way data partitioning (training, validation, and test sets), and classification performance was assessed primarily by the precision-recall area under the curve (PR-AUC) to correct for class imbalance. Marker sets achieving PR-AUC ≥ 0.7 in the test dataset were retained as high-performing, yielding 945 predictive signatures. This threshold was selected to ensure clinical relevance and avoid overfitting [28]. Random Forest (RF) and Extreme Gradient Boosting (XGB) models were then applied in parallel to the 945 signatures. Cross-model evaluation compared AUC, PR-AUC, accuracy, sensitivity, specificity, precision, and F1-score, leading to the identification of 119 consistently robust signatures with overfitting. Pie charts illustrate the proportional contribution of each annotation method to the final marker pool. To validate stability, each signature was trained and tested using five random seeds (Figure 5C-a). AUC distributions across partitions confirmed consistent model behavior. Overfitting was assessed by PR_AUC differences between validation and test classifying signatures categories - None, Mild, Moderate, or Severe (Figure 5C-b). Among the 945 candidates, 29.5% showed no overfitting, 32.5% mild, 37.4% moderate, and only 0.6% severe. Performance metrics, including precision (Figure 5C-c), recall (Figure 5C-d), and F1 score (Figure 5C-e), declined progressively with increasing overfitting severity, as indicated by lower medians and broader distributions. Yellow bars denote mean performance within each category. To compare

algorithmic consistency, we analyzed overfitting-free (None) signatures across both RF and XGB models (Figure 5D). All six performance metrics-AUC, accuracy, sensitivity, specificity, precision, and F1 score – showed strong inter-model correlation, confirming robust, model-independent predictive capacity. Performance variations among all signatures were further visualized using stratified boxplots and (Supplementary Figure Classification performance declined modestly from None to Severe groups, with AUC and F1 scores showing the steepest reductions, while specificity and precision remained relatively stable (Supplementary Figure S5A-a, S5B-a). Heatmaps of normalized performance metrics highlighted clusters top-performing signatures, and the top 20 signatures for RF and XGB were ranked and visualized (Supplementary Figure S5A-b, S5B-b). Comprehensive datasets are provided in Supplementary Tables S5-1 to S5-3, including the full list of predictive gene signatures with gene composition and partitioning results across random seeds (S5-1), detailed RF/XGB performance metrics (S5-2), and overfitting classification for each signature (S5-3).

Composite scoring identifies robust gene signatures predictive of metastatic prostate cancer and reveals clinical correlations

To systematically evaluate gene signatures predictive of metastatic status (M0 vs. M1), we analyzed 119 candidate gene signatures constructed from scRNA-seq-derived DEGs. For each signature, a composite score was computed as the averaged performance from RF and XGB models. Based on these scores, 55 positive and 64 negative signatures were identified (Figure 6A; Supplementary Table S6-1-1). Applying all 119 signatures to bulk RNA-seq data, we visualized M-stage classification outcomes via heatmap (Figure 6B). Signatures were ranked by composite score, with individual predictions shown per sample (M0: blue; M1: red). Among them, 19 signatures achieved mean accuracy ≥0.65, including five ≥0.7 (Supplementary Table S6-1-2), indicating strong predictive potential. Subsequently, all possible combinations (Combos) of 2-5 gene signatures from these top 19 were tested to assess whether integration improves prediction relative M-stage single-signature models. The cellular origins of the 19 top-performing signatures were then analyzed. Based on inclusion of epithelial (KRT18) and immune (PTPRC) markers, signatures were classified as Include or Exclude.

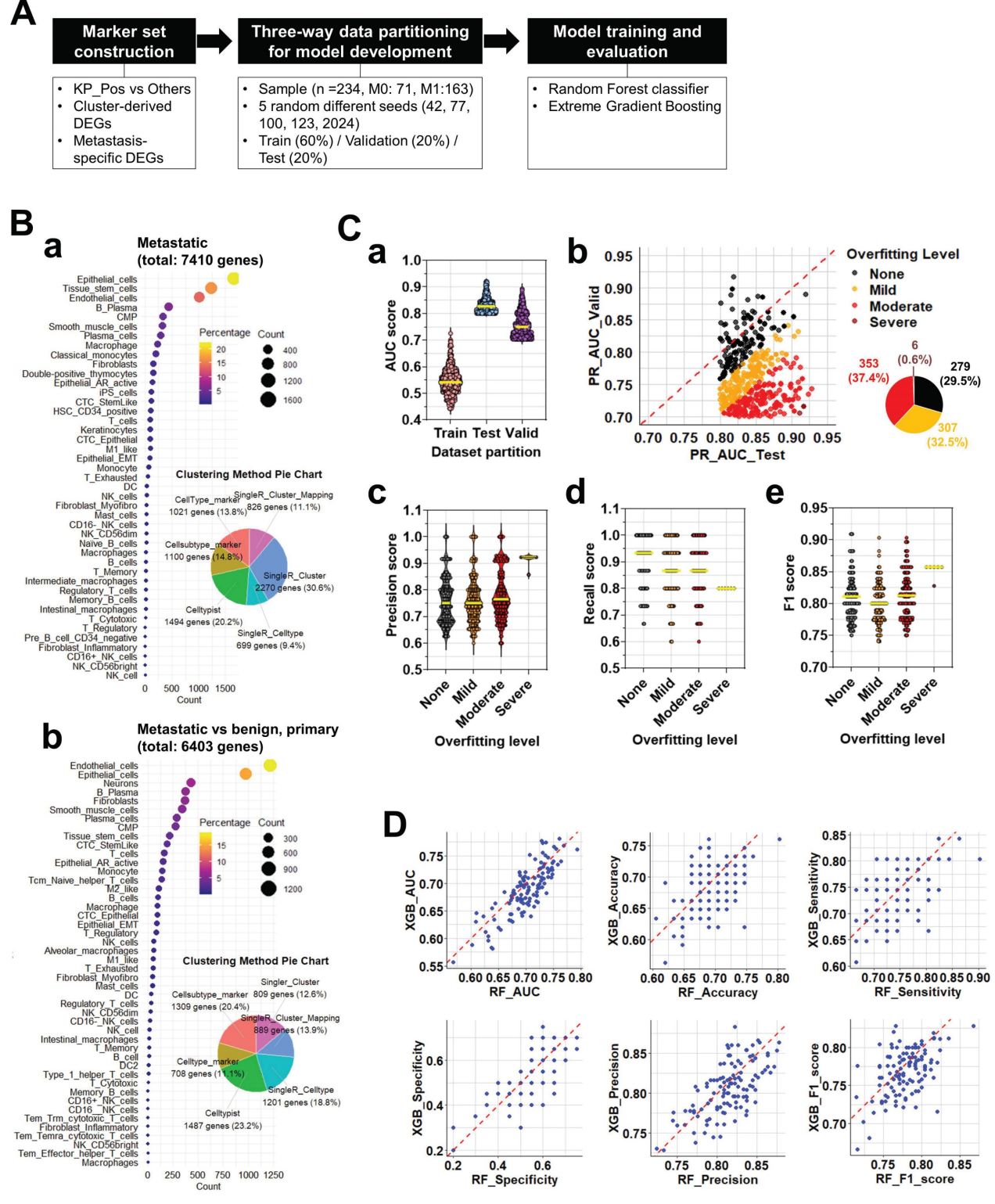


Figure 5. Construction and evaluation of predictive signatures for M0/M1 classification based on differentially expressed genes. (A) Workflow for signature evaluation. Step 1: Marker set construction using cluster-derived DEGs and metastasis-specific DEGs identified from cell-level annotation strategies. Step 2: Three-way data partitioning for model development using bulk RNA-seq data combined with clinical information. Five independent random seeds were applied for reproducibility analysis. Step 3: Signature validation through model training and evaluation using Random Forest (RF) and Extreme Gradient Boosting (XGB) algorithms. (B) Composition of the marker Pool. (a) Cell type and clustering method-dependent distribution of cluster-derived DEGs. The left panel shows a bubble plot summarizing the number of DEGs per cell type across annotation methods. The right pie chart displays proportional contributions from each method (SingleR, CellTypist, etc.). (b) Cell type and clustering method-dependent distribution of metastasis-specific DEGs. The left panel shows a bubble plot summarizing DEGs derived from metastasis-specific comparisons, while the right pie chart shows contributions from each method. (C) Three-way data partitioning analysis for model development. (a) AUC scores for training, validation, and test datasets. (b) Overfitting level evaluation of signatures, based on the difference between PR_AUC in validation and test sets. Scatter plot with pie chart summarizes the proportion of signatures categorized as none, mild, moderate, or severe overfitting. (c) Precision scores of signatures according to overfitting level. (e) PI scores of signatures according to overfitting level. Yellow horizontal lines indicate the average score within each group. (D) Comparative performance of RF and XGB models using signatures from the none overfitting group. Eight scatter plots display the correlation between RF and XGB models in terms of AUC, accuracy, sensitivity, specificity, precision, and FI score for signatures clas

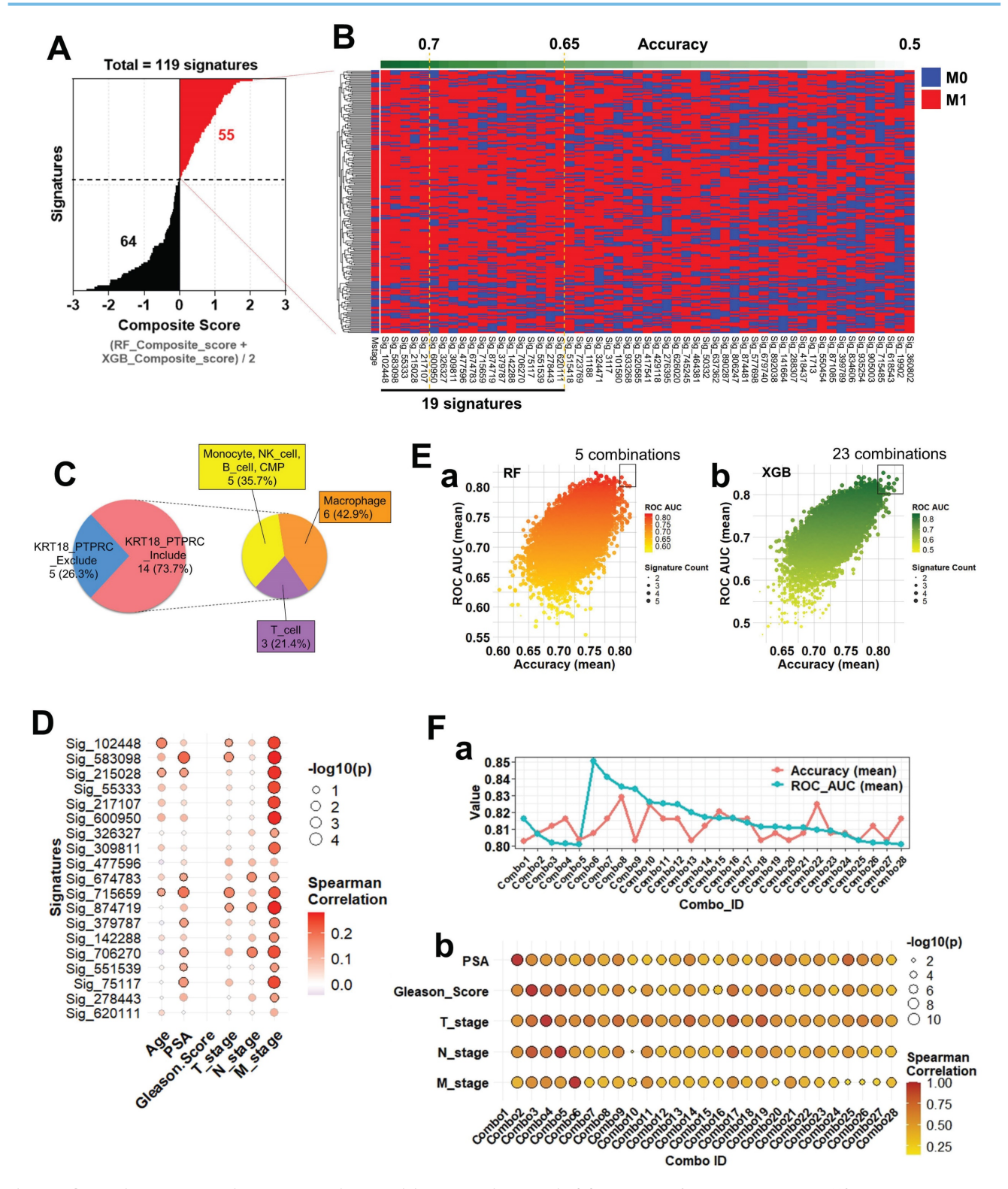


Figure 6. Composite score-based signature evaluation and clinical correlation analysis. (A) Distribution of composite scores across 119 gene signatures predictive of metastatic status (M0 vs. M1). Composite scores were calculated as the average of RF and XGBoost-derived scores. Among them, 55 signatures with positive composite scores (red) and 64 with negative scores (black) were identified. (B) Heatmap illustrating M-stage prediction (M0: blue, M1: red) across bulk RNA-seq samples using the 119 signatures, sorted by composite score. The top-performing signatures (accuracy ≥ 0.7, n = 5; accuracy ≥ 0.65, n = 19) are highlighted. (C) Cell-of-origin analysis for the 19 signatures with accuracy ≥ 0.65. Based on the presence of KRT18 and/or PTPRC, signatures were grouped into 'Include' or 'Exclude'. The 'Include' group was further classified into three cell-type categories: (1) monocyte, NK cell, B cell, and CMP (35.7%), (2) macrophage (42.9%), and (3) T cell (21.4%). (D) Spearman correlation between individual signature scores (top 19) and clinical variables (Age, PSA, Gleason Score, T_stage, N_stage, M_stage). Circle color represents correlation strength, size reflects −log₁₀(p-value), and circles with black outlines indicate statistical significance (p < 0.05). (E) Prediction performance of multi-signature combinations assessed using (a) RF and (b) XGB models. Here, "combinations" refer to all possible sets of 2 to 5 signatures drawn from the top 19 signatures identified in panel B. Each dot corresponds to a unique combination, with color denoting ROC AUC signatures drawn from the top 19 signatures identified in panel B. Each dot corresponds to a unique combination was derived from the top 19 signatures (2–5 signatures per combination). a. Line plots showing average accuracy (red) and average ROC AUC (blue) for each combination across the test dataset. b. Correlation analysis between combined signature scores and clinical parameters. Dot size indicates −log₁₀(p-value), color represents correlation coefficien

The majority (73.7%) belonged to Include, macrophage subdivided into $(42.9\%)_{i}$ monocyte/NK/B cell/CMP (35.7%), and T cell (21.4%) subgroups (Figure 6C), indicating meaningful contributions from both immune- and epithelialderived genes. Prediction heterogeneity across the full 945 signatures was visualized using heatmaps (Supplementary Figure S6-1). Considerable variability was observed, yet lineage-based grouping revealed that monocyte-, NK-, B cell-, and CMP-derived Include signatures exhibited classification patterns comparable to macrophage- and T cell-derived ones, underscoring their robustness. To assess clinical relevance, we performed Spearman correlation analysis between signature scores and clinical parameters (Age, PSA, Gleason Score, T_stage, N_stage, and M_stage). Most predictive signatures correlated significantly with M stage (Figure 6D), and particularly Sig_583098 and Sig_715659 also showed associations with PSA and T_stage, supporting their clinical utility as metastasis-related biomarkers. Next, we tested whether combining multiple signatures enhances prediction accuracy. Ensemble models using RF (Figure 6E-a) and XGB (Figure 6E-b) evaluated diverse signature combinations. Each dot in the scatterplots represents one unique combination, with dot size indicating the number of signatures and color denoting ROC AUC. Several combinations achieved ROC AUC > 0.8, demonstrating the advantage of multi-signature integration (Supplementary Tables S6-2-1 and S6-2-2). Selected combinations were further validated for accuracy and clinical correlation. Multiple combinations maintained high test-set accuracy and ROC AUC (Figure 6F-a). Correlation analyses (Figure 6F-b) revealed significant associations with Gleason Score, T_stage, and M stage, confirming both robustness and clinical interpretability. Interestingly, Combo 1, despite strong M-stage prediction, showed no correlation with clinical parameters, suggesting that it captures metastasis-linked transcriptomic features independent of conventional variables.

Discussion

Metastasis remains the leading cause of mortality among men with prostate cancer (PCa), and reliable prediction of metastatic potential remains a major unmet clinical need. In this study, we investigated the transcriptomic and spatial characteristics of hybrid circulating tumor cell (CTC)-like cells co-expressing epithelial (KRT18) and immune (CD45/PTPRC) markers, termed KP_Pos, to elucidate their origin and clinical significance. Through integrated Imaging Mass Cytometry (IMC), single-cell RNA sequencing (scRNA-seq), and bulk

RNA-seq-based modeling, we identified lineagespecific transcriptomic programs and gene signatures associated with metastasis and demonstrated their predictive power in stratifying patients by metastatic status.

Spatial IMC analysis of metastatic prostate tumor microenvironments revealed close proximity and frequent interaction between CK⁺ epithelial and CD45⁺ immune cells, coinciding with the emergence of CK⁺CD45⁺ hybrid phenotypes. Although such cells have been linked to fusion-related enlargement [9, 29], our morphometric profiling revealed an opposite pattern: CK+CD45+ double-positive cells in CK-high tumors (Group 1) were smaller yet more abundant than in other groups, with size distributions shifted toward compact morphologies (Figure 2B-c,d). These compact phenotypes, observed across multiple lineage markers (CD14, CD16, CD3, CD8A, Granzyme, Perforin), likely represent metabolically active states rather than quiescence, consistent with small but functionally potent CD45RO+ memory T cells and CD16⁺ NK cells [30, 31]. IMC quantification confirmed enrichment of activation and checkpoint molecules (CD25, HLA-DR, PD-1) in these compact hybrids, aligning with evidence that morphologically small circulating cells increase in advanced disease and predict poor prognosis [32]. Collectively, these findings suggest that KP_Pos cells are compact, active immune-epithelial hybrids engaged in tumorimmune communication rather than simple fusion products. Consistently, CellChat analysis (Figure 2C) demonstrated that epithelial cells acted as both senders and receivers of intercellular signals with monocytes and T cells, underscoring a bidirectional epithelial-immune signaling network in KP_Pos emergence.

In PBMC scRNA-seq from M1-stage metastatic PCa patients, KP_Pos T cells exhibited a distinct expression profile marked by KRT18 and multiple ribosomal genes (RPS12, RPS13, RPL30, RPS3A, RPL11, RPL32, RPS8, RPS23, RPS14, RPL5), indicating partial epithelial-like reprogramming possibly driven by tumor-derived factors or extracellular vesiclemediated transcript transfer [33]. Enhanced ribosomal expression implies increased translational capacity and adaptation to circulatory stress [34], whereas downregulation of mitochondrial oxidative phosphorylation (OXPHOS) genes (MT-CO1, MT-CO2, MT-CO3, MT-ATP6, MT-ND5) regulators (PARP8, RABGAP1L, UTRN, ZEB2) indicates metabolic rewiring toward glycolytic states linked to T-cell exhaustion [35, 36]. These data suggest that KP_Pos T cells constitute metabolically altered, transcriptionally hybrid subsets imprinted by tumor-derived molecular signals [37]. Similar

epithelial-like gene patterns appeared across other immune lineages: B cells co-upregulated KRT18, RPS12, RPL9, RPS19, RPL8, RPL12, RPS18, RPS17, and stress-related genes RASSF7 and PLIN3, suggesting cytoskeletal and lipid metabolic adaptation [38, 39]; monocytes induced KRT18, PEF1-AS1, and SLCO1B3, indicating xenobiotic responsiveness [40, 41]; and platelets showed unexpected KRT18, S1PR2, CDK5R1, TET1, and PMS2/PMS2P3 upregulation, reflecting epithelial transcript uptake or intercellular RNA transfer [42]. These convergent profiles across immune subsets support a systemic tumor-immune molecular exchange, generating shared hybrid programs (Figures transcriptional 1, Supplementary Figures S1-S4; Supplementary Tables S3-1 to S3-6).

Within metastatic tumor scRNA-seq datasets, multiple annotation approaches (SingleR, CellTypist, marker-based mapping) confirmed the presence of KP Pos cells across immune (macrophages, monocytes, T cells) and epithelial compartments. Transcriptomic comparisons revealed enrichment of immune-response, antigen-presentation, epithelial-mesenchymal transition (EMT) pathways, suggesting biological-not artifactual-origins. Dual validation at protein and transcript levels (IMC and scRNA-seq) confirmed KRT18/CD45 co-expression (Supplementary Figures S1-1C, S2-3). The distribution of KP Pos cells differed by context: circulating PBMC hybrids localized mainly within T and B cells, while tissue-resident KP_Pos cells (Figures 3-4) included NK, macrophage, epithelial, and stromal subsets, reflecting microenvironmental pressures that drive hybrid diversity.

Functional enrichment analyses (Supplementary Figures S6-2, S6-3-1-S6-3-9) revealed consistent enrichment of immune, antigen-presentation, and EMT pathways, consistent with evidence that the TME promotes stemness and therapy resistance [43], that EMT activation correlates with immune evasion [44, 45], and that EMT-related transcriptional programs predict poor outcomes [46]. Reports that transcriptionally primed cells can drive lymph node-independent metastasis [47] further support KP_Pos cells as metastasis-competent intermediates.

From these data, we derived 945 lineage-specific gene signatures and assessed metastatic classification performance using Random Forest (RF) and Extreme Gradient Boosting (XGB) models. Several individual achieved signatures ≥0.7 accuracy, while combinations of top-performing signatures reached ≥0.8, indicating additive predictive value (Figures 5-6). The use of multiple clustering and annotation methods was essential to capture hybrid diversity and prevent bias toward dominant lineages

(Supplementary Figures S5A–B, S6-1; Supplementary Tables S5-1 to S5-3, S6-1-1, S6-1-2, S6-2-1, S6-2-2; Reference 26). These predictive signatures bridge molecular characteristics of primary tumors and CTC-like hybrids, supporting the concept that primary tumor transcriptional states can inform metastatic potential. The existence of CD45⁺/KRT⁺ hybrid CTCs in advanced prostate and breast cancers [10, 11] reinforces this biological continuum linking tumor-immune interaction and systemic dissemination.

Several limitations must be acknowledged. All analyses were based on a single internal cohort. External validation using TCGA PRAD SU2C_PRAD datasets was limited by differences in sequencing platforms and gene coverage (TCGA_ PRAD: 20,531 genes; SU2C_PRAD: 19,293 genes; our dataset: 36,553 genes), which precluded complete model transfer and prevented direct testing of our predictive signatures without compromising integrity (Figures 5-6; Supplementary Tables S5-1 to S5-3, S6-1-1, S6-1-2, S6-2-1, S6-2-2). Moreover, scRNA-seq primarily detects upregulated genes due to dropout effects [48], yet these transcripts remain the most [49-51]. reliable for signature generation Discrepancies between single-cell and bulk RNA-seq data reflect inherent differences in resolution and have been similarly reported in other studies [51-53]. Although panCK⁺/CD45⁺ CTC-like cells were detected in the blood of 45 metastatic prostate cancer patients, standardized enrichment protocols and independent validation of their prognostic utility beyond PSA and Gleason score will be essential in future prospective and longitudinal studies.

Conclusion

Our study establishes the existence and clinical relevance of CD45+CK18+ (PTPRC+KRT18+) hybrid CTC-like cells in metastatic prostate cancer. By linking their emergence to epithelial-immune signaling, metabolic remodeling, and EMT programs, we identify predictive gene signatures capable of distinguishing metastatic status with high accuracy. These findings provide a framework for non-invasive biomarker development, illuminate the biology of immune-epithelial plasticity, and suggest new therapeutic opportunities targeting hybrid-cell formation. Nevertheless, as this study was based on cross-sectional transcriptomic data longitudinal survival analysis, the causal and prognostic roles of KP_Pos cells remain to be clarified.

Abbreviations

AUC: Area under the curve; CD45: Cluster of Differentiation 45, also known as Leukocyte Common

Antigen (LCA); CK: cytokeratin; CMP: Common myeloid progenitor; CTC: Circulating tumor cell; DEG: Differentially expressed gene; EMT: Epithelialmesenchymal transition; IMC: Imaging Mass Cytometry; KP Pos: KRT18⁺PTPRC⁺ (CD45⁺KRT18⁺); KRT18: Cytokeratin 18; M0: No distant metastasis detected; M1: Distant metastasis present; Macro: macrophage; Mono: monocyte; mPCa: metastatic prostate cancer; MT-ATP6: Mitochondrially Encoded ATP Synthase Membrane Subunit 6; MT-CO1: Mitochondrially Encoded Cytochrome c Oxidase I; MT-CO2: Mitochondrially Encoded Cytochrome c Oxidase II; MT-CO3: Mitochondrially Encoded Cytochrome c Oxidase III; MT-ND5: Mitochondrially Encoded NADH: Ubiquinone Oxidoreductase Core Subunit 5; NK: Natural killer; PanCK: Pan-Cytokeratin; PARP8: Poly(ADP-Ribose) Polymerase Family Member 8; PBMC: Peripheral blood mononuclear cell; PCa: Prostate cancer; PR-AUC: Precision-recall area under the curve; PSA: Prostate-specific antigen; PSMA: Prostate-specific antigen; PTPRC: Protein phosphatase receptor type C, a gene encoding CD45; RABGAP1L: RAB GTPase Activating Protein 1 Like; RF: random forest; ROC AUC: Receiver operating characteristic area under the curve; RPL11: Ribosomal Protein L11; RPL30: Ribosomal Protein L30; RPL32: Ribosomal Protein L32; RPL5: Ribosomal Protein L5; RPS12: Ribosomal Protein S12; RPS13: Ribosomal Protein S13; RPS14: Ribosomal Protein S14; RPS23: Ribosomal Protein S23; RPS3A: Ribosomal Protein S3A; RPS8: Ribosomal Protein S8; TME: Tumor microenvironment; TNM stage: Tumor-Node-Metastasis stage; t-SNE: t-distributed Stochastic Neighbor Embedding; UTRN: Utrophin; Vim: vimentin; XGB: Extreme Gradient Boosting; ZEB2: Zinc Finger E-box Binding Homeobox 2.

Supplementary Material

Supplementary figures and tables. https://www.thno.org/v16p1594s1.zip

Acknowledgments

Funding

This study was supported by the Ministry of Education of the Republic of Korea and the National Research Foundation of Korea (NRF) grant funded by the Korean government (MSIT) (2022R1A2C3005586; PIs: J.S. Lee and H.H. Han), the National Cancer Center Grant (NCC-2211880-3; PI: J.Y. Joung), and the Korea Health Industry Development Institute (KHIDI) through the Global Physician-Scientist Training Program (formerly the K-Medi Convergence

Talent Training Program) (RS-2024-00440041; PI: H.H. Han), Republic of Korea.

Data availability

The raw and processed RNA-seq data generated in this study are publicly available in the Gene Expression Omnibus (GEO) under accession numbers GSE297652 and GSE297742. All additional datasets, including gene expression matrices, annotation resources, and model results, are provided as Supplementary Data. Raw sequencing data that are not publicly available due to ethical or institutional restrictions may be made available by the corresponding authors upon reasonable request.

Author contributions

Baek Gil Kim and Yeonsue Jang contributed equally as co-first authors, primarily responsible for study design, data analysis, data visualization, and drafting of the manuscript. Min Gyu Kim collected and curated single-cell RNA sequencing (scRNA-seq) datasets. Dongwook Song contributed to bulk RNA-seq data collection and short-read sequencing, supporting comparative transcriptomic analyses. Jungchan Jung assisted with bulk RNA-seq data acquisition and Imaging Mass Cytometry (IMC) sample preparation. Jihee Jung and Ayoung Yoo coordinated clinical sample acquisition contributed to clinical metadata integration. Hyeong Jung Woo and Woon-Hae Kim performed circulating cell analysis. Jongsoo Lee provided oversight of clinical sample collection, clinical management, and project funding. Minseok S. Kim and Hyun Young Shin supervised circulating cell analysis and related project components. Nam Hoon Cho, as a pathologist and IMC expert, led IMC data analysis and interpretation. Hyun Ho Han and Jae Joung supervised the project co-corresponding authors, contributing to validation of the results, overall project management, and securing funding. All authors reviewed and approved the final version of the manuscript.

Competing Interests

A patent application related to this work (Korean Patent Application No. 10-2025-0112412), filed in collaboration with Yonsei University, has been submitted and is currently pending. The authors declare this as a potential conflict of interest.

References

 Sung H, Ferlay J, Siegel RL, Laversanne M, Soerjomataram I, Jemal A, et al. Global Cancer Statistics 2020: GLOBOCAN Estimates of Incidence and Mortality Worldwide for 36 Cancers in 185 Countries. CA Cancer J Clin. 2021; 71(3): 209-249.

- Mottet N, van den Bergh RCN, Briers E, Van den Broeck T, Cumberbatch MG, De Santis M, et al. EAU-EANM-ESTRO-ESUR-SIOG Guidelines on Prostate Cancer-2020 Update. Part 1: Screening, Diagnosis, and Local Treatment with Curative Intent. Eur Urol. 2021; 79(2): 243-262.
- Siegel RL, Miller KD, Wagle NS, Jemal A. Cancer statistics, 2023. CA Cancer J Clin. 2023; 73(1): 17-48.
- Nicholson C, Vela I, Williams ED. Prostate Cancer Metastasis. In: Welch DR, editor. Introduction to Cancer Metastasis. Cambridge, MA: Academic Press; 2017. p. 33-59.
- Shore ND, Moul JW, Pienta KJ, Czernin J, King MT, Freedland SJ. Biochemical recurrence in patients with prostate cancer after primary definitive therapy: treatment based on risk stratification. Prostate Cancer Prostatic Dis. 2024; 27(2): 192-201.
- Yamada Y, Beltran H. The treatment landscape of metastatic prostate cancer. Cancer Lett. 2021; 519: 20-29.
- Kim SH, Jeong CW, Do MT, Han JH, Jeong SH, Yuk HD, et al. Changes in treatment after gallium-68 prostate-specific membrane antigen-11 positron emission tomography/computed tomography in patients with prostate cancer: a retrospective case series study. J Urol Oncol. 2024; 22(2): 157–165.
- Cieslikowski WA, Antczak A, Nowicki M, Zabel M, Budna-Tukan J. Clinical Relevance of Circulating Tumor Cells in Prostate Cancer Management. Biomedicines. 2021; 9(9): 1179.
- Manjunath Y, Porciani D, Mitchem JB, Suvilesh KN, Avella DM, Kimchi ET, et al. Tumor-Cell-Macrophage Fusion Cells as Liquid Biomarkers and Tumor Enhancers in Cancer. Int J Mol Sci. 2020; 21(5): 1872.
- Reduzzi C, Gerratana L, Zhang Y, D'Amico P, Shah AN, Davis AA, et al. CK+/CD45+ (dual-positive) circulating cells are associated with prognosis in patients with advanced breast cancer. J Clin Oncol. 2022; 40(16_suppl): 1093. Meeting Abstract: 2022 ASCO Annual Meeting.
- Woo HJ, Kim WH, Shin HY, Jung H, Lee HH, Kim MS, et al. CD45 positive circulating tumor cells as a prognostic marker in prostate cancer. Clin Cancer Res. 2024; 30(21_Suppl): A003. Meeting Abstract: Biology Behind Circulating Tumor Cells (CTCs), Nov 13, 2024.
- Gast CE, Silk AD, Zarour L, Riegler L, Burkhart JG, Gustafson KT, et al. Cell fusion potentiates tumor heterogeneity and reveals circulating hybrid cells that correlate with stage and survival. Sci Adv. 2018; 4(9): 20217828
- Dietz MS, Sutton TL, Walker BS, Gast CE, Zarour L, Sengupta SK, et al. Relevance of circulating hybrid cells as a non-invasive biomarker for myriad solid tumors. Sci Rep. 2021; 11(1): 13630.
- Patel RK, Parappilly M, Farley HC, Latour EJ, Wang LG, Nair AM, et al. Circulating Neoplastic-Immune Hybrid Cells Are Biomarkers of Occult Metastasis and Treatment Response in Pancreatic Cancer. Cancers (Basel). 2024; 16(21): 3650.
- Ali AM, Raza A. scRNAseq and High-Throughput Spatial Analysis of Tumor and Normal Microenvironment in Solid Tumors Reveal a Possible Origin of Circulating Tumor Hybrid Cells. Cancers (Basel). 2024; 16(7): 1444.
- 16. Yang C, Wang X, To KKW, Cui C, Luo M, Wu S, et al. Circulating tumor cells shielded with extracellular vesicle-derived CD45 evade T cell attack to enable metastasis. Signal Transduct Target Ther. 2024; 9(1): 84.
- 17. Wu X, Yan H, Qiu M, Qu X, Wang J, Xu S, et al. Comprehensive characterization of tumor microenvironment in colorectal cancer via molecular analysis. Elife. 2023; 12: e86032.
- Han H, Kang M, Byun SS, Yun SJ. Genetic testing for prostate cancer, urothelial cancer, and kidney cancer. J Urol Oncol. 2023; 21(2): 128-139.
- Su Z, Zhong Y, He Y, You L, Xin F, Wang L, et al. Bulk- and single cell-RNA sequencing reveal KIF20A as a key driver of hepatocellular carcinoma progression and immune evasion. Front Immunol. 2024; 15: 1469827.
- Zhong C, Yang D, Zhong L, Xie W, Sun G, Jin D, et al. Single-cell and bulk RNA sequencing reveals Anoikis related genes to guide prognosis and immunotherapy in osteosarcoma. Sci Rep. 2023; 13(1): 20203.
- Yazdani A, Lenz HJ, Pillonetto G, Mendez-Giraldez R, Yazdani A, Sanoff H, et al. Gene signatures derived from transcriptomic-causal networks stratify colorectal cancer patients for effective targeted therapy. Commun Med (Lond). 2025; 5(1): 9.
- Mundi PS, Dela Cruz FS, Grunn A, Diolaiti D, Mauguen A, Rainey AR, et al. A Transcriptome-Based Precision Oncology Platform for Patient-Therapy Alignment in a Diverse Set of Treatment-Resistant Malignancies. Cancer Discov. 2023; 13(6): 1386-1407.
- 23. Woo HJ, Kim SH, Kang HJ, Lee SH, Lee SJ, Kim JM, et al. Continuous centrifugal microfluidics (CCM) isolates heterogeneous circulating tumor cells via full automation. Theranostics. 2022; 12(8): 3676-3689.
- Woo HJ, Rademacher PN, Shin HY, Lee J, Intisar A, Warkiani ME, et al. Robust Automated Separation of Circulating Tumor Cells and Cancer-Associated Fibroblasts for Enhanced Liquid Biopsy in Breast Cancer. Anal Chem. 2025; 97(32): 17452-17461.

- Liao K, Zhang X, Liu J, Teng F, He Y, Cheng J, et al. The role of platelets in the regulation of tumor growth and metastasis: the mechanisms and targeted therapy. MedComm (2020). 2023; 4(5): e350.
- Le Chapelain O, Jadoui S, Gros A, Barbaria S, Benmeziane K, Ollivier V, et al. The localization, origin, and impact of platelets in the tumor microenvironment are tumor type-dependent. J Exp Clin Cancer Res. 2024; 43(1): 84.
- 27. Van Dam S, Krijgsman D, Kucukkose E, Verdonschot MEL, Amini M, Blokx WAM, et al. Anti-PD-1 treatment response is associated with the influx of circulating myeloid and T-cell subsets into the metastatic melanoma tumor microenvironment. Br J Cancer. 2025: [in press].
- Mandrekar JN. Receiver operating characteristic curve in diagnostic test assessment. J Thorac Oncol. 2010; 5(9): 1315-1316.
- Sutton TL, Patel RK, Anderson AN, Bowden SG, Whalen R, Giske NR, et al. Circulating Cells with Macrophage-like Characteristics in Cancer: The Importance of Circulating Neoplastic-Immune Hybrid Cells in Cancer. Cancers (Basel). 2022; 14(16).
- Andreatta M, Tjitropranoto A, Sherman Z, Kelly MC, Ciucci T, Carmona SJ. A CD4(+) T cell reference map delineates subtype-specific adaptation during acute and chronic viral infections. Elife. 2022; 11: e76339.
- Bujko A, Atlasy N, Landsverk OJB, Richter L, Yaqub S, Horneland R, et al. Transcriptional and functional profiling defines human small intestinal macrophage subsets. J Exp Med. 2018; 215(2): 441-458.
- Sun Q, Li W, Yang D, Lin PP, Zhang L, Guo H. The Presence of Small-Size Circulating Tumor Cells Predicts Worse Prognosis in Non-Small Cell Lung Cancer Patients. Arch Pathol Lab Med. 2025; 149(1): 39-49.
- Clancy JW, D'Souza-Schorey C. Tumor-Derived Extracellular Vesicles: Multifunctional Entities in the Tumor Microenvironment. Annu Rev Pathol. 2023; 18: 205-229.
- 34. Albert B, Kos-Braun IC, Henras AK, Dez C, Rueda MP, Zhang X, et al. A ribosome assembly stress response regulates transcription to maintain proteome homeostasis. Elife. 2019; 8: e45002.
- Lindstrom MS. Emerging functions of ribosomal proteins in gene-specific transcription and translation. Biochem Biophys Res Commun. 2009; 379(2): 167-170.
- Chapman NM, Chi H. Metabolic rewiring and communication in cancer immunity. Cell Chem Biol. 2024; 31(5): 862-883.
- Griffiths JI, Wallet P, Pflieger LT, Stenehjem D, Liu X, Cosgrove PA, et al. Circulating immune cell phenotype dynamics reflect the strength of tumor-immune cell interactions in patients during immunotherapy. Proc Natl Acad Sci U S A. 2020; 117(27): 16072-16082.
- 38. Zheng X, Dong Q, Zhang X, Han Q, Han X, Han Y, et al. The coiled-coil domain of oncogene RASSF 7 inhibits hippo signaling and promotes non-small cell lung cancer. Oncotarget. 2017; 8(45): 78734-78748.
- He Y, Liu L, Dong Y, Zhang X, Song Y, Jing Y, et al. Lipid droplets-related Perilipin-3: potential immune checkpoint and oncogene in oral squamous cell carcinoma. Cancer Immunol Immunother. 2024; 73(5): 78
- 40. Wu S, Qi Y, Yang W. The Noncanonical Functions of Metabolites in Tumor Progression. Metabolites. 2024; 14(3): 171.
- Qiu H, Liang J, Yang G, Xie Z, Wang Z, Wang L, et al. Application of exosomes in tumor immunity: recent progresses. Front Cell Dev Biol. 2024; 12: 1372847.
- 42. Rowley JW, Schwertz H, Weyrich AS. Platelet mRNA: the meaning behind the message. Curr Opin Hematol. 2012; 19(5): 385-391.
- Nallasamy P, Nimmakayala RK, Parte S, Are AC, Batra SK, Ponnusamy MP. Tumor microenvironment enriches the stemness features: the architectural event of therapy resistance and metastasis. Mol Cancer. 2022; 21(1): 225.
- 44. Wang G, Xu D, Zhang Z, Li X, Shi J, Sun J, et al. The pan-cancer landscape of crosstalk between epithelial-mesenchymal transition and immune evasion relevant to prognosis and immunotherapy response. NPJ Precis Oncol. 2021; 5(1): 56.
- Imodoye SO, Adedokun KA. EMT-induced immune evasion: connecting the dots from mechanisms to therapy. Clin Exp Med. 2023; 23(8): 4265-4287.
- Li Y, Li K, Wang H, Qiu J, Xiao C. Identification of epithelial-mesenchymal transition prognostic signature associated with prognosis, tumor microenvironment, and therapeutic effect in prostate cancer. Front Genet. 2025; 16: 1539745.
- Zheng C, Zhu B, Chen Y, Shahid N, Hu Y, Ali Husain HMA, et al. Integrating proteomics and machine learning reveals characteristics and risks of lymph node-independent distant metastasis in colorectal cancer. Front Immunol. 2025; 16: 1622528.
- Qiu P. Embracing the dropouts in single-cell RNA-seq analysis. Nat Commun. 2020; 11(1): 1169.

- Pullin JM, McCarthy DJ. A comparison of marker gene selection methods for single-cell RNA sequencing data. Genome Biol. 2024; 25(1):
- 50. Ianevski A, Giri AK, Aittokallio T. Fully-automated and ultra-fast cell-type identification using specific marker combinations from single-cell transcriptomic data. Nat Commun. 2022; 13(1): 1246.
- 51. Stuart T, Butler A, Hoffman P, Hafemeister C, Papalexi E, Mauck WM, 3rd, et al. Comprehensive Integration of Single-Cell Data. Cell. 2019; 177(7): 1888-1902. e21.
- 52. Zhou S, Lin N, Yu L, Su X, Liu Z, Yu X, et al. Single-cell multi-omics in the study of digestive system cancers. Comput Struct Biotechnol J. 2024; 23: 431-445.
- 53. Wu X, Yang X, Dai Y, Zhao Z, Zhu J, Guo H, et al. Single-cell sequencing to multi-omics: technologies and applications. Biomark Res. 2024; 12(1): 110